An article presented by Professors Luke T. Roling and Jean-Philippe Tessonnier from Iowa State University, United States.

Structure sensitivity of the electrochemical hydrogenation of *cis,cis*-muconic acid to hexenedioic acid and adipic acid

The electrocatalytic conversion of *cis,cis*-muconic acid to adipic acid was demonstrated with high selectivity for the first time over supported palladium catalysts. A combined computational and experimental approach uncovered the role of terrace sites in driving catalytic activity, identifying a mechanism that incorporates sequential outer-sphere proton-coupled electron transfer and surface-mediated electrocatalytic hydrogenation.

Image by Ella Maru Studio.

As featured in:

ROYAL SOCIETY
OF **CHEMISTRY**

rsc.li/greenchem

PAPER

Check for updates

Structure sensitivity of the electrochemical hydrogenation of *cis,cis*-muconic acid to hexenedioic acid and adipic acid†

Deep M. Patel, [ID] ‡[a,b] Prathamesh T. Prabhu, [ID] ‡[a,b] Geet Gupta,[a,b]
Marco Nazareno Dell'Anna, [ID] [a,b] Samantha Kling,[a,b] Huy T. Nguyen,[a,b]
Jean-Philippe Tessonnier [ID] ⋆[a,b] and Luke T. Roling [ID] ⋆[a,b]

The global market of fossil carbon-derived adipic acid (AA) was over 3 million tons in 2022, emitting 3.1 million tons of the potent greenhouse gas N_2O. Alternative biomass-derived feedstocks offer a sustainable option to replace fossil carbon, but alternative pathways for AA synthesis are also required to curb the substantial emissions associated with the process. A novel and sustainable approach to synthesize AA is by coupling biomanufacturing and electrocatalysis. Biologically-produced *cis,cis*-muconic acid (*cc*MA) from sugars and lignin monomers has recently gained significant attention as a precursor to AA, as it can be electrochemically hydrogenated to AA using water-derived (instead of fossil-derived) hydrogen and electricity generated from wind energy. For the first time in literature, we demonstrate appreciable electrochemical production of AA using supported palladium nanoparticles. The performance of this system contrasts with that of palladium foil or platinum-based catalysts, which produced little AA. Density functional theory calculations on model surfaces of palladium and platinum suggest that the reduction of *cc*MA to *trans*-3-hexenedioic acid occurs through an outer sphere proton-coupled electron transfer mechanism, while subsequent reduction to AA preferentially occurs on surface terrace sites. Our calculations also explain the exceptional performance of palladium nanoparticles compared to palladium- and platinum-based foils, attributing the more favorable activation energy barriers found on palladium terraces to the relatively moderate binding strength of adsorbed species. These results suggest structure-sensitive catalyst design strategies that maximize the exposure of terrace atoms for further improvement of the *cc*MA electrochemical hydrogenation process.

Introduction

Replacing fossil hydrocarbons with renewable feedstocks such as lignocellulosic biomass has recently gained significant traction in chemical production.[1–4] However, the decarbonization of the chemical industry also requires significant process innovation to reduce water and energy usage and minimize waste production, in accordance with the United Nations Sustainable Development Goals.[5] Adipic acid (AA) production from petroleum-based cyclohexane is one of the largest chemi-

cal processes in terms of annual volumetric turnover, and is accordingly one of the most significant greenhouse gas (GhG) emitting processes.[6–8] The global production of AA exceeded 3 million tons in 2022 with an annual growth of 3–5%; this production emits 3.1 million tons of N_2O, a greenhouse gas 300 times more potent than CO_2.[9,10] About 75% of AA produced is utilized in the synthesis of Nylon-6,6, a commodity polymer broadly used in the packaging, textile, and automotive industries.[11–14] Due to the unmatched chemical and mechanical properties and the large market size of nylons, it is difficult to replace nylon with a bio-based polymer like polylactic acid.[15] Therefore, innovation is needed to make nylon synthesis more sustainable.

The current commercial approach to synthesize AA is through oxidation of petroleum-derived cyclohexane in the presence of air and nitric acid.[16,17] Recent efforts to develop greener routes for AA production have focused on replacing cyclohexane with lignin-derived phenol;[18] however, the overall process to obtain ketone-alcohol oil from phenol is costly and

a Department of Chemical and Biological Engineering, Iowa State University, Ames, IA 50011, USA. E-mail: roling@iastate.edu, tesso@iastate.edu
b Center for Biorenewable Chemicals (CBiRC), Ames, IA 50011, USA

‡ These authors contributed equally to this work.

environmentally unfriendly.[19] *cis,cis*-Muconic acid (*cc*MA) has gained significant attention as a biomass-derived platform intermediate to synthesize AA.[20–24] Recent studies have shown promising results to sustainably produce high concentrations of *cc*MA in a single-step batch fermentation process.[25,26] Notably, PTT Global Chemical has reported *cc*MA titers as high as 81.5 g L^{-1} from lignocellulosic biomass, motivating further research on developing sustainable pathways for its conversion to commodity chemicals.[27] *cc*MA, a C$_6$-diunsaturated dicarboxylic acid, can be thermocatalytically hydrogenated to AA on conventional Re, Pt, and Pd-based catalysts with appreciable turnover frequencies (TOFs) and nearly 100% selectivity to AA at >90% conversion of MA.[28–31] However, the thermocatalytic pathway requires a high pressure of H$_2$ (4–10 bar)[30] typically produced by methane steam reforming, another GhG emission-intensive process.

Electrocatalysis is of emerging significance due to its operation at ambient reaction conditions, its ability to utilize renewably-sourced electricity for generating current, the relative ease of modulating the reaction driving force through the cell potential, and the use of water as a source of hydrogen.[32,33] However, as summarized in Fig. 1, previous studies have shown that *cc*MA electrochemical hydrogenation (ECH) to AA was surprisingly challenging, and instead selectively produced the monounsaturated diacid *trans*-3-hexenedioic acid (*t*3HDA).[33–35] Such monounsaturated acids have been recently shown to find applications in synthesizing performance-advantaged nylons.[36]

In this study, we demonstrate for the first time that *cc*MA ECH can be driven to form AA with high selectivity on commercial Pd/C under acidic conditions. These results contrast with results on commercial Pt/C, which yielded smaller concentrations of AA with slower kinetics, and Pd and Pt foils, which only produced *t*3HDA. Density functional theory (DFT) calculations suggest that the exceptional activity on Pd/C could be due to an abundance of terrace sites, which bind adsorbed

species relatively moderately and exhibit the lowest activation energies for *cc*MA ECH to AA. Our results further suggest an interplay between processes occurring in the outer sphere, forming monounsaturated diacids, and the further reaction of those species on the catalyst surface to form AA. Interestingly, the proposed electrochemical pathway is different from the previously proposed thermocatalytic pathway on Pd/C, which highlights the reaction environment-sensitive nature of the *cc*MA reduction mechanism.[31] Our cyclic voltammograms combined with DFT calculations further show that the effect of coadsorbed organic molecules on HER onset potential is sensitive to the identity of the catalyst surface. Overall, this work is the first report on hydrogenating *cc*MA to AA using protons in solution as a green alternative to fossil-fuel derived H$_2$ gas, demonstrating the promise of using ECH to open new pathways for the sustainable production of monomers from biomass-derived feedstocks.

Results and discussion

Screening Pd and Pt catalyst geometries for electrochemical hydrogenation of *cis,cis*-muconic acid

Since Pd and Pt-based catalysts[33,34] were observed to achieve substantial conversions and TOFs of MA to AA *via* thermocatalytic hydrogenation,[29,30] we started by screening different geometries (foils *vs.* nanoparticles) of Pd- and Pt-based catalysts for *cc*MA ECH through chronoamperometry (CA) in acidic media (Fig. 2 and Fig. S1–S3†). During this screening process,

Fig. 1 Overview of the current state of the art for *cis,cis*-muconic acid (*cc*MA) electrochemical hydrogenation under acidic conditions. Solid arrows are for experimentally demonstrated pathways, and dotted arrows are for energetically possible pathways based on DFT calculations. Black text is for previously explored catalyst materials, and the blue text is for materials explored in this study. Notation: *t*3HDA: *trans*-3-hexenedioic acid, *t*2HDA: *trans*-2-hexenedioic acid, AA: adipic acid. Red H atoms are those added during ECH.
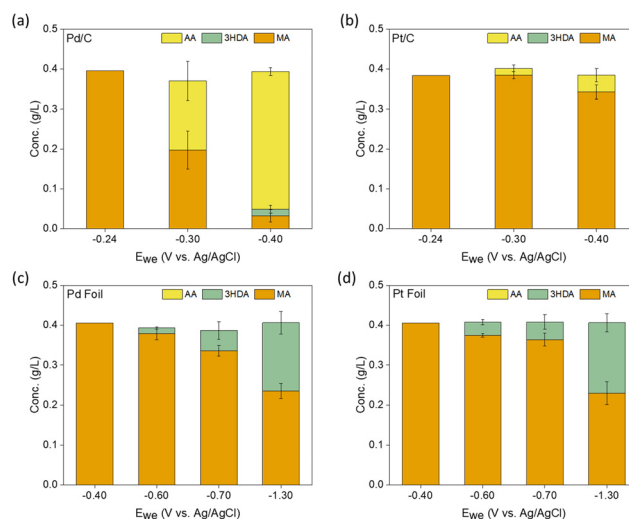
Fig. 2 Concentration (g L^{-1}) of reactants and products in solution after 1 hour of chronoamperometry (CA) experiments performed at varying working potentials (E_{we}) on (a) Pd/C, (b) Pt/C, (c) Pd foil, and (d) Pt foil. The error bars represent the standard error from triplicates. In addition to these products, we observed a small concentration (0.1 g L^{-1}) of muconolactone (not shown here for simplicity) that remained constant throughout the course of the reaction on all materials and at all potentials (see Methods section and Fig. S1–S3† for more details). Notation: MA: muconic acid, 3HDA: *trans*-3-hexenedioic acid, AA: adipic acid.

we found surprisingly high activity on Pd nanoparticles (TOF$_{MA}$: 1.1 s^{-1}, ccMA conversion after 1 h: 91%) with high selectivity (>95%, faradaic efficiency (FE): 18%) at −0.4 V vs. Ag/AgCl (V$_{Ag/AgCl}$). Based on the constant voltage bulk electrolysis experiments for higher catalyst loading (10 mg), we observe 100% conversion and selectivity to AA on Pd/C and Pt/C (Fig. S4†). These observations, combined with DFT calculations in the following section, identify t3HDA and t2HDA as reaction intermediates to form AA. Such high yield of AA on Pd/C suggests that the final process design for synthesizing bio-based AA might not require complicated downstream separation processes.

Pt nanoparticles were considerably less active (TOF$_{MA}$: 0.1 s^{-1}, ccMA conversion after 1 h: 12%) and less selective for ECH (AA selectivity: >90%, FE: 3%) than Pd nanoparticles. In contrast to the results on nanoparticles, Pd and Pt foils did not produce any AA, yielding t3HDA as the only hydrogenation product with poor FE (<5%), in good agreement with previous observations.[34]

The relatively low FE observed for the best catalytic performance (18% on Pd/C) suggests that ~80% of the cathodic current is being used in the production of H$_2$ gas. While this observation provides a motivation for future studies to fine-tune reaction conditions for Pd/C to reduce HER,[37] or design catalyst materials with high hydrogen overpotential,[38] the co-produced H$_2$ could be stored locally and used in fuel cells to compensate for the intermittent nature of wind energy.[39,–41]

We performed constant-current experiments to verify that the observed product distribution in Fig. 2 is not an artifact of differences in mass-transfer kinetics across different materials. As shown in Fig. S5,† at a current density of 5 mA cm^{-2} we observe high selectivity and conversion of ccMA to AA on Pd nanoparticles. In contrast, on foils we observe t3HDA as a sole product with low ccMA conversion (<10% after 1 h) on Pd foil. Increasing the current densities from 5 mA cm^{-2} to 50 mA cm^{-2} and 100 mA cm^{-2} on Pd foil enhanced the production of the hydrogenation reaction but had no effect on its product selectivity, i.e., t3HDA remained the sole product on Pd foil. These observations suggest that mass-transfer kinetics are not affecting the product distributions.

Density functional theory calculations for cis,cis-muconic acid hydrogenation on (111) and (533) surfaces of Pd and Pt

We performed DFT calculations to understand the different activities of ccMA ECH on foils and nanoparticles. We first investigated the reaction mechanism on Pd(111) and Pt(111) surfaces to understand reaction energetics on highly coordinated terrace surface sites. Fig. 3 summarizes the key elementary steps along with the corresponding reaction free energies (ΔG) and activation free energies (G$_a$); energetics are calculated at −0.14 V vs. the reversible hydrogen electrode (V$_{RHE}$), equivalent to −0.40 V$_{Ag/AgCl}$ at the relevant experimental conditions. A summary of all the elementary steps that were considered is provided in Fig. S6.† Adsorption of ccMA is thermodynamically favorable on (111) surfaces, with adsorption free energies of −1.91 eV for Pd(111) and −2.01 eV for Pt

(111). However, the activation free energies for ccMA* hydrogenation to its preferred single-hydrogenation intermediate (cMAH-2ad*, Fig. 3) were relatively high (Pd: 0.82 eV, Pt: 0.40 eV). We therefore anticipate that the first hydrogenation will more readily occur through a non-catalytic outer-sphere mechanism in the solution (ΔG = 0.08 eV) at the considered potential. Although the radical cMAH-2ad species could adsorb on the surface (Pd: −1.83 eV, Pt: −2.18 eV), we anticipate that it also is more readily hydrogenated in solution to trans-2-hexenedioic acid (t2HDA) or t3HDA because of the similarly large activation free energies on the surface to form t2HDA* (Pd: 0.57 eV, Pt: 0.80 eV) or t3HDA* (Pd: 0.69 eV, Pt: 0.85 eV), whereas the formation of t2HDA or t3HDA in solution are highly favored energetically (more than 1 eV energetically downhill). This comparison of activation energies on the surface with free energies in solution provides only a qualitative picture of the relative reactivities of the surface and solution processes. We do not exclude the prospect of the surface forming t2HDA* or t3HDA* solely on the basis of the calculations, as calculating appropriate activation energies in the solution phase would be computationally expensive to perform accurately. We do note, however, the activation energies required to perform ECH to t2HDA or t3HDA on the surface (each requiring overcoming a barrier of at least 0.80 eV for an elementary hydrogenation step) are much larger than anticipated activation barriers for H$_3$O$^+$ dissociation (~0.08 eV)[42] and therefore we anticipate surface-mediated steps to be relatively difficult. These conclusions are consistent with our recent experimental studies showing that these steps can occur as outer-sphere PCET processes, with similar rates and selectivity for Pb, Bi, Pd, and Pt foils suggesting that the step is not directly surface-mediated.[33,35]

The reaction free energies for further reduction of t2HDA (0.66 eV) and t3HDA (0.64 eV) in solution are substantially more positive. In these cases, the activation energies of surface-mediated t2HDA* hydrogenation on Pd(111) (0.39 eV) and Pt(111) (0.48 eV) are both lower than the solution-phase reaction free energy. We therefore anticipate the most favorable ECH of t2HDA occurs by adsorbing on the (111) surface (−0.63 eV for Pd, −1.11 eV for Pt) before the third and fourth elementary hydrogenations. The activation free energies for t3HDA* ECH are relatively higher (Pd: 0.77 eV; Pt: 1.16 eV), making the solution-phase reaction energetics more competitive. However, given that we observe AA on nanoparticles but not on foils (Fig. 2), we believe that t3HDA ECH most likely is a surface-catalyzed process. We further note that a more favorable pathway for t3HDA* ECH to AA may occur by isomerization on the surface to t2HDA*, with maximum activation free energies corresponding to H-abstraction (0.58 eV on Pd(111) and 1.04 eV on Pt(111)). t2HDA* will more readily undergo further ECH than desorb, explaining why it is not observed experimentally.

We note that Pt(111) generally binds species more strongly than Pd(111); for example, t2HDA and t3HDA bind stronger on Pt(111) by 0.48 eV and 0.51 eV, respectively. We also find that the activation free energy barriers are 0.1–0.4 eV higher on
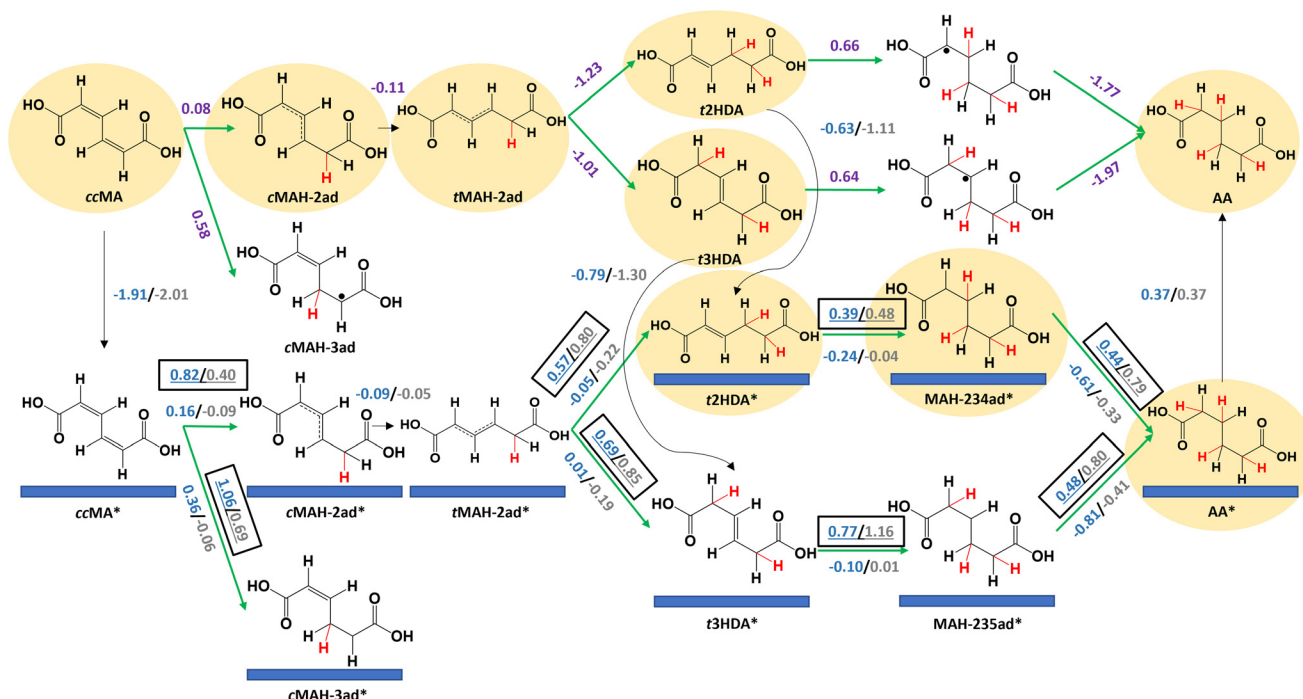
Fig. 3 Reaction energetics at −0.14 V_{RHE} and 298 K for elementary steps in electrochemical hydrogenation of *cis,cis*-muconic acid (*cc*MA) to *trans*-2-hexenedioic acid (*t*2HDA), *trans*-3-hexenedioic acid (*t*3HDA), and adipic acid (AA) on Pd(111) [blue], Pt(111) [grey], and in solution [purple]. Green arrows denote electrochemical steps and black arrows denote non-electrochemical steps. Activation free energies (G_a, eV) are underlined and boxed; reaction free energies (ΔG, eV) are also provided (not underlined or boxed). The H atoms added to *cc*MA during ECH are highlighted in red for clarity. "*" denotes adsorbed species. "." denotes an unpaired electron. The species involved in the energetically preferred pathway are highlighted.

Pt(111) than on Pd(111) for steps after *t*2HDA* or *t*3HDA* adsorption, explaining the relatively poor experimental ECH activity to AA on Pt surfaces. This behavior is related to the tendency of stronger binding surfaces such as Pt to favor bond breaking, leading bond-making ECH steps to have higher barriers on such surfaces.[43] This result is qualitatively similar to that in previous literature for benzaldehyde ECH, which suggested that Pd/C is significantly more active than Pt/C due to relatively low activation barriers for ECH of organic species on Pd.[44]

Finally, we calculate a slightly positive desorption free energy of 0.37 eV for AA* on Pd(111) and Pt(111), which is relatively weaker than the other species and easily overcome at the reaction conditions.[34] Moreover, this adsorption strength is likely overestimated, as it is calculated according to Hess's law to close the thermodynamic cycle (see Methods section).[45] Overall, the reaction energetics suggest the most favorable ECH pathway occurs by *cc*MA forming *t*2HDA/*t*3HDA in solution with AA produced by surfaces, and that the higher activity of Pd(111) stems from its overall lower activation energies along that pathway. Alternative free energy diagrams comparing Pd(111) and Pt(111) surface energetics are provided in Fig. S7 and S8.†

We next calculated reaction energetics on Pd(533) and Pt (533) surfaces to understand the effects of undercoordinated atoms at step edges on *cc*MA ECH (Fig. 4). As was the case on (111) surfaces, the reaction energetics suggest that *cc*MA ECH

to *t*2HDA/*t*3HDA occurs through an outer-sphere mechanism due to the high activation energies associated with the corresponding surface reactions. The adsorption free energies of *t*2HDA (Pd(533): −1.29 eV; Pt(533): −1.72 eV) and *t*3HDA (Pd (533): −1.46 eV; Pt(533): −1.91 eV) are more favorable than on the corresponding (111) surfaces. However, the activation energies associated with the subsequent surface-mediated steps are substantially higher than on the corresponding (111) surfaces, again consistent with the principle that stronger-binding surfaces generally have higher barriers for bond-making steps. We therefore anticipate that stepped surfaces are relatively inactive for *cc*MA ECH (in particular, the ECH of *t*2HDA and *t*3HDA) due to their strong-binding nature. Free energy diagrams comparing Pd(533) and Pt(533) surface energetics are provided in Fig. S9 and S10.†

Our current computational approach does not differentiate between the energetics of Langmuir–Hinshelwood-type or Eley–Rideal-type mechanisms,[46,47] for the purpose of simplicity within the scope of this work. The quantification of relative flux through these mechanisms is limited by our model, including crucial effects such as quantifying surface coverage effects and solvent–adsorbate interactions. We note that dissociation of H_3O^+ will have a small activation barrier[42] (~0.08 eV) relative to other calculated barriers, and therefore, we believe that its implicit treatment by focusing primarily on reaction free energies of solution phase steps is appropriate.[48]
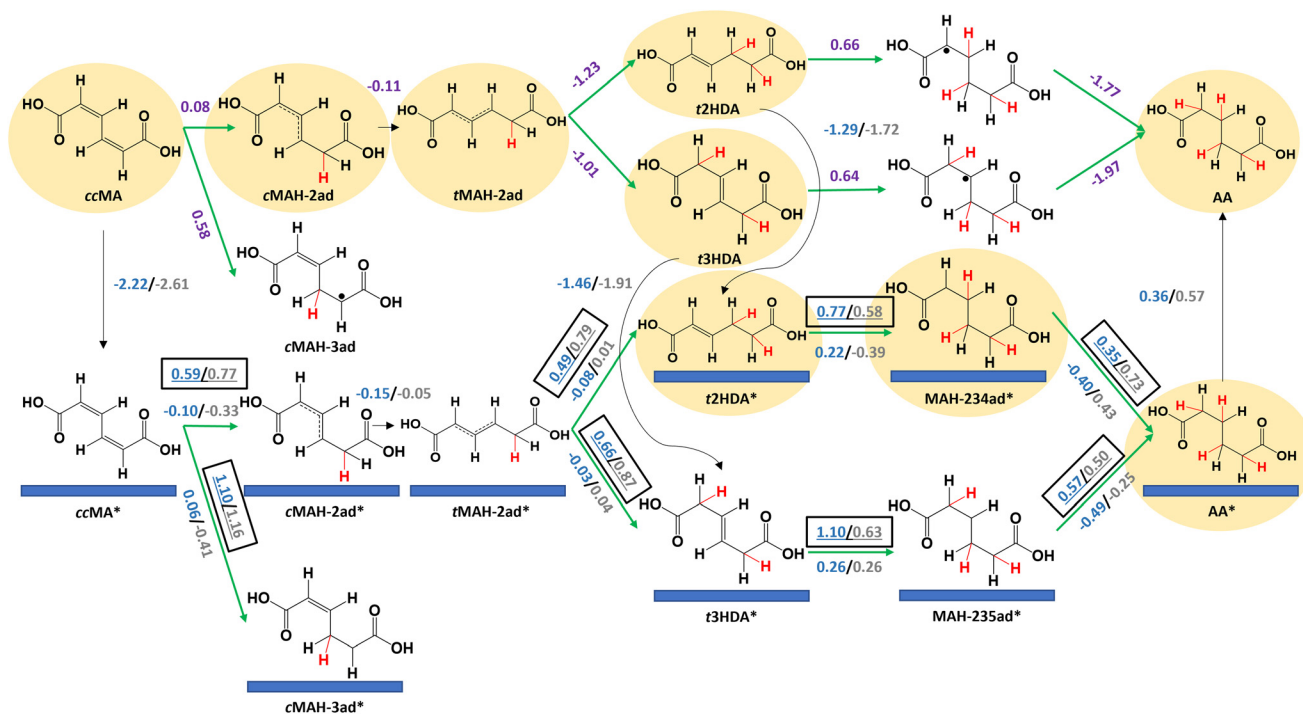
Fig. 4 Reaction energetics at −0.14 V_{RHE} and 298 K for elementary steps in electrochemical hydrogenation of *cis,cis*-muconic acid (*cc*MA) to *trans*-2-hexenedioic acid (*t*2HDA), *trans*-3-hexenedioic acid (*t*3HDA), and adipic acid (AA) on Pd(533) [blue], Pt(533) [grey], and in solution [purple]. Green arrows denote electrochemical steps and black arrows denote non-electrochemical steps. Activation free energies (G_a, eV) are underlined and boxed; reaction free energies (ΔG, eV) are also provided (not underlined or boxed). The H atoms added to *cc*MA during ECH are highlighted in red for clarity. "*" denotes adsorbed species. "." denotes an unpaired electron. The species involved in the energetically preferred pathway are highlighted.

We have not explicitly accounted for the effect of solvent, counterions, electrical double layer, surface charge effects, or coverage effects (*e.g.*, effects of coadsorbed H*/other ions, water molecules, and organic species) in our surface calculations to maintain a reasonable computational cost in this mechanistic study. We acknowledge that this might impact the quantitative nature of our assessment, and note that some of these effects (*e.g.*, interfacial electric field) might have appreciable effects on the absolute reaction energetics.[49,50]

Determining the relative barriers for *trans*-2-hexenedioic acid *vs.* *trans*-3-hexenedioic acid hydrogenation for adipic acid production

Our DFT results in Fig. 3 and 4 suggest that the hydrogenation of *cc*MA to AA proceeds sequentially through pathways that involve monounsaturated intermediates *t*2HDA and *t*3HDA. Therefore, to experimentally understand and validate these concepts, we performed constant-current bulk electrolysis experiments at −100 mA starting with *t*3HDA and *t*2HDA model solutions on Pd/C (Fig. 5).

Since *t*2HDA is not commercially available, we synthesized it through base-catalyzed isomerization of *t*3HDA following a procedure reported previously.[51] This method produces a mixture (HDA$_{mix}$) of *t*2HDA (70–80%) and *t*3HDA (10–20%). Higher *t*2HDA concentrations could not be achieved due to the reaction's thermodynamic equilibrium. Separation of *t*2HDA
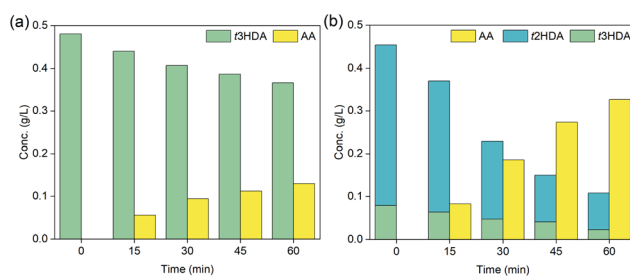

Fig. 5 Concentration (g L^{-1}) of *trans*-2-hexenedioic acid (*t*2HDA), *trans*-3-hexenedioic acid (*t*3HDA) and adipic acid (AA) with reaction time (min) for constant-current (−100 mA) bulk electrolysis using (a) *t*3HDA, and (b) HDA$_{mix}$ model solutions on Pd/C.

also proved to be challenging as both isomers show similar chemical and physical properties. Nevertheless, the significantly higher concentration of *t*2HDA in the mixture compared to *t*3HDA enabled us to study its reactivity for the first time.

From Fig. 5, we note that both HDA intermediates were readily hydrogenated to AA on Pd/C with no trace of other hexenedioic acid isomers, which indicates that *t*2HDA to *t*3HDA isomerization (or *vice versa*) in solution is unlikely under ECH conditions. The reaction rate was also significantly faster for the *t*2HDA and *t*3HDA mixture compared to pure *t*3HDA, which is in line with DFT-calculated lower activation energies

(eV) for t2HDA* hydrogenation (Pd(111): 0.39, Pd(533): 0.77) compared to t3HDA* hydrogenation (Pd(111): 0.77, Pd(533): 1.10) on Pd.

Understanding the effect of organic intermediates on hydrogen desorption characteristics at Pd- and Pt-based materials

Previously, Singh et $al.$[52] quantified the adsorption of organics based on the charge calculation in the underpotential deposited hydrogen (H_{UPD}) region using a Pt wire electrode. They observed competitive adsorption between organics including phenol, benzaldehyde, and cyclohexanol $vs.$ H^+ at low concentrations of organics (0.01 M), and almost all the H_{UPD} sites were blocked at higher concentrations. Further, Yu et $al.$[53] recently showed that biomass-based organic molecules like furfural can exhibit coverage-dependent competitive adsorption with H*, due to differences in the adsorption geometries of furfural. Therefore, we calculated adsorption free energies of H* to determine how they change in the presence of organics. Our DFT results show that the adsorption of H* becomes less favorable on each surface in the presence of ccMA*, t2HDA*, and t3HDA*, with the following ranges of destabilization on each surface: Pd(111) 0.38–0.46 eV; Pd(533) 0.14–0.46 eV; Pt(111) 0.22–0.30 eV; Pt(533) 0.18–0.29 eV. To experimentally investigate this effect at foils and nanoparticles, we performed cyclic voltammetry (CV) measurements using respective model solutions, explained in detail in the Experimental section. The potential was swept between −0.25 $V_{Ag/AgCl}$ and 1.25 $V_{Ag/AgCl}$, where ccMA and its intermediates are not active for ECH. Fig. 6 shows the H_{UPD} adsorption/desorption peaks in the 0.0 to −0.25 $V_{Ag/AgCl}$ range on Pt foil.
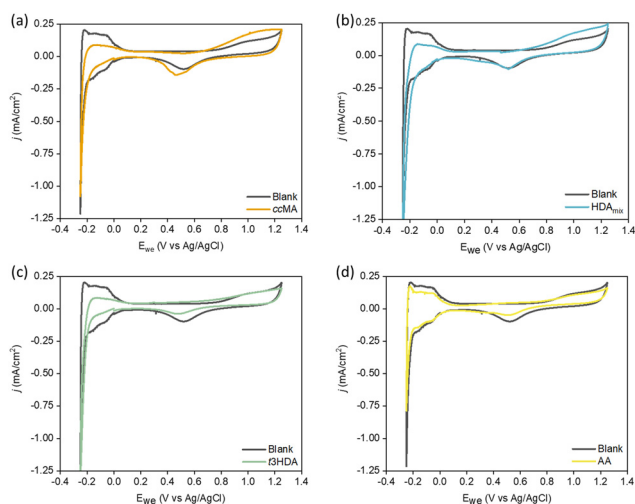

Fig. 6 Cyclic voltammograms for model solutions containing (a) cis, cis-muconic acid (ccMA), (b) HDA$_{mix}$, (c) $trans$-3-hexenedioic acid (t3HDA), and (d) adipic acid (AA), along with 0.1 M H_2SO_4 (blank) solution reference on polycrystalline Pt foil. The peak near 0.6 $V_{Ag/AgCl}$ is characteristic of PtO$_x$ reduction, and those in the range of 0.0 to −0.2 $V_{Ag/AgCl}$ are characteristic peaks for H* adsorption/desorption. The scan rate for obtaining CVs was 50 mV s^{-1}.

CVs performed on the model solutions containing ccMA (Fig. 6a), HDA$_{mix}$ (Fig. 6b), and t3HDA (Fig. 6c) showed suppression of $H_{desorption}$ peaks. In comparison, the model solution containing AA (Fig. 6d) did not show any changes in the CV. The low solubility limit of ccMA and its intermediates limits the complete blockage of Pt sites. Unlike Pt foil, Pd foil (Fig. S11†) does not show any facet-specific $H_{adsorption/desorption}$ peaks, but only one prominent peak for $H_{desorption}$. Overall, from Fig. S11–S13,† we observe a similar trend across all materials with approximately the same percent suppression of H_{UPD} peak for strong binding organics such as MA and HDA. These CVs combined with DFT calculations hint at the presence of competitive adsorption between H^+ and respective organic species, except in cases of weakly binding organics like AA.

To determine the relative interplay between ccMA ECH and HER at foils and NPs, we performed linear sweep voltammetry (LSV) for respective model solutions at Pd/Pt foils and Pd/Pt carbon-supported nanoparticles (Fig. S14†). The LSV currents were normalized by the metallic surface area calculated using CO chemisorption for the supported metal nanoparticles, and the geometric surface area for the foils. The current transients observed for blank samples were purely HER. Comparing the onset potentials of HER in the presence and absence of organics on Pt foils (Fig. S14a†) and Pt NPs (Fig. S14b†), we note that the presence of organics does not change the onset potential of HER on either of these Pt-based materials.

Together, these observations suggest that the presence of organics or the structure of Pt and Pd surface do not significantly impact the thermodynamic driving force for HER under acidic conditions on the Pt and Pd surfaces studied in this work. Overall, while these observations on Pt surfaces are in line with previous AIMD calculations by Yuk et $al.$ which showed that Pt(111) does not have a strong impact of the presence of an organic on the HER activity, our observations contrast with their findings on Pd(111) which showed suppression of HER activity in the presence of strong binding organics.[54] Finally, we did not detect any differences in the onset potential of HER for blank solutions on Pd- and Pt-based materials (Fig. S14†).

Implications for catalyst design

Our computational results demonstrated that while t3HDA most likely forms via an outer-sphere electrochemical process, the subsequent formation of AA likely occurs on the surface as the activation energy barriers are significantly lower for those ECH steps. Further, the structure sensitivity of t3HDA activation is significant, as terraces ($e.g.$, (111) surface facets) are likely to be much more active for AA formation than undercoordinated step edges due to the overbinding nature of step edges. Our experimental results showed that Pd/C (and, to a lesser extent, Pt/C) nanoparticles were active for AA formation, in contrast to the corresponding foils that yielded only t3HDA. We therefore anticipate the commercial Pd/C and Pt/C catalysts contain a relatively high fraction of terrace-like atoms on their

surfaces, while the foils contain a high proportion of under-coordinated step atoms.

We investigated the nature of Pd and Pt metal foils and supported nanoparticles using X-ray diffraction (XRD) (Fig. 7). We note that XRD is not a surface-sensitive technique and that its information depth typically ranges between 1 and 10 μm.[55] However, prior studies have shown excellent correlations between XRD and surface-sensitive techniques (*e.g.*, EBSD) in the case of commercial Pd and Pt foils.[55,56] Here, we combine our X-ray diffractograms with TEM images (Fig. S15†) and previous EBSD-based arguments for these materials to comment on the exposed surface facets. The X-ray diffractograms of foils showed mainly (220) step reflections with trace amounts of (111) and (200) terrace reflections, which is characteristic of the orientation of its fcc structure. These reflections are consistent with XRD and EBSD results obtained independently by other groups; the predominance of high-index facets was attributed to the sheer forces applied during the cold rolling of Pd foils.[55–57] Further, Yule *et al.* recently showed that HER is relatively more facile on higher index facets such as (411), compared to that on lower-index facets including (100), (111), and (110).[58] Combining this observation with our X-ray diffracto-

grams and the high FE of HER (>95%) on our polycrystalline foils, we anticipate a relatively larger fraction of higher index facets on our polycrystalline Pd and Pt foils. As an additional validation, we compared the CV of our polycrystalline Pt foil (Fig. 6) with those reported by Marković *et al.*,[59] which suggest that our polycrystalline Pt foil has (100), (111), and (110) type facets. Specifically, we observe a slightly larger current density for the (110) characteristic peak at -0.22 $V_{Ag/AgCl}$ compared to that for other coupled characteristic peaks of (111) and (100) facets in the range of -0.01 to -0.12 $V_{Ag/AgCl}$, which supports our claim of relative abundance of steps compared to terraces on polycrystalline foils.

In contrast, our X-ray diffractograms for Pd/C and Pt/C display reflections higher along the (111), and (200) facets, which are characteristic of the fcc crystal of Pd (or Pt), consistent with literature.[60] Combining these X-ray diffractograms with the *d*-spacing determined from the TEM image of Pd/C (Fig. S15†), we infer that our Pd/C and Pt/C have relatively higher exposure of terraces than the corresponding foils. Overall, these observations are therefore consistent with our DFT-predicted notion that the improved activity of our nanoparticle catalysts is due to a high exposure of terrace sites on those materials. Combining this prediction with our CA results (Fig. 2), our experimental and computational work suggest that terraces are more active than steps for MA ECH to AA. This finding contrasts with previous literature,[61] which suggested that the ECH of aliphatic ketones is more favorable on undercoordinated sites of Pt-group metals than on the respective terraces.

We performed preliminary tests to determine the recyclability of the Pd/C catalyst, using the same catalyst for 3 consecutive ECH runs held at a constant potential of -0.40 $V_{Ag/AgCl}$ for 1 hour. These showed that the catalyst deactivates over time (Fig. S16†), consistent with literature on Pd/C for formic acid electro-oxidation.[62] Mitigating this deactivation is beyond the scope of the present work and will be a topic of future studies.

Our results demonstrate the benefit of structure-sensitive catalyst design strategies for these reactions. The higher activity of (111) facets motivates the exploration and use of catalyst materials selectively exposing such faces, such as Pd octahedra.[63] Future catalyst design efforts should also explore the effects of adsorbate binding; our calculations suggested that weaker binding of adsorbates is beneficial for reducing activation energies for AA formation, though it is still to be determined whether weakening binding relative to that on Pd (111) would continue to enhance activity by lowering activation energies, given the need to activate C=C bonds (*i.e.*, finding the peak of an activity "volcano" plot). Finally, improved catalysts would continue to mitigate HER activity while reducing dependence on precious metal components.

Fig. 7 X-ray diffractograms of Pd/C, Pd foil, Pt/C, and Pt foil before reaction. Color code: metal (blue), carbon (pink), PdO (green).

Conclusions

The use of electrocatalysis to drive the next generation of sustainable chemical transformations requires atomic-scale inno-
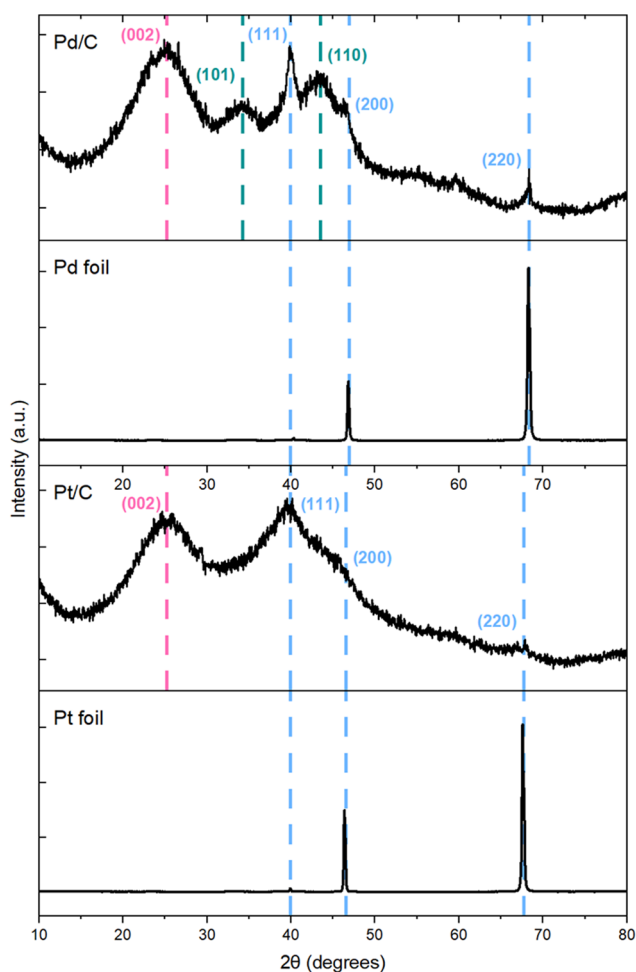
vation and insight to design systems with suitable activity and selectivity to desired products. We here provide the first report in the literature of appreciable AA production from ccMA ECH using Pd nanoparticles. This contrasts with small to no AA activity on Pt nanoparticles, and production of only t3HDA on Pd and Pt foils. Using computations, we obtain an atomic-scale understanding of ccMA ECH towards t2HDA, t3HDA, and AA at terraces and undercoordinated steps of Pd and Pt. DFT-calculated reaction energetics suggest that the initial reduction of ccMA → t2HDA/t3HDA might be happening through an outer-sphere mechanism; this is corroborated by the lack of significant change observed experimentally in the onset potential of ccMA ECH on foils or nanoparticles of Pd and Pt. In contrast, the subsequent reduction of the monounsaturated acids to AA likely proceeds through a surface-mediated pathway at the catalyst surface. DFT calculation combined with constant-current bulk electrolysis experiments further suggest that t2HDA reacts faster than t3HDA to form AA, which may explain the lack of t2HDA observed in bulk electrolysis products. DFT calculations predict that terraces are more active than steps for the formation of AA due to the substantially lower activation energies found on (111) surfaces; this combined with XRD analysis suggests the higher activity of Pd/C nanoparticles relative to foil is due to a relative abundance of terrace-like surface atoms compared to foils. Experimental CVs suggest the presence of competitive adsorption between H^+ and organics at metal–electrolyte interface; LSVs show no detectable change in the HER onset in the presence of organics on Pt- or Pd-based materials. Together, these results suggest structure-sensitive catalyst design strategies employing selective exposure of terrace atoms and modulation of surface binding strength to further reduce activation energy barriers and yield high ECH activity.

Experimental details

Computational details

Plane-wave DFT calculations were performed using the Vienna *ab initio* simulation package (VASP).[64,65] Electron–ion interactions were quantified by projector augmented wave (PAW) potentials.[66,67] Exchange correlations were calculated using Perdew–Burke–Ernzerhof (PBE) functionals.[68] The zero-damped DFT-D3 method was implemented to apply dispersion corrections.[69,70] Dipole corrections were applied in the *z*-direction normal to the surface.[71] The kinetic energy cutoff was set to 400 eV, with electronic convergence calculated to 10^{-4} eV.

Calculations on (111) surfaces were performed using a $5 \times 5 \times 4$ periodic unit cell; those on (533) surfaces were performed with a $4 \times 5 \times 4$ periodic unit cell. Metal atoms in the bottom two layers of all the slabs were fixed at their respective bulk positions; all other atoms, including adsorbates, were fully relaxed. A $4 \times 4 \times 1$ Monkhorst–Pack *k*-point grid[72] was used for these surface calculations; the grid was gamma-centered on (111) surfaces. At least 14 Å of vacuum spacing was used between periodic images. DFT-calculated lattice constants of bulk Pd and Pt were used to construct all slab models (experimental values[73] are

provided in parentheses, all values in Å): Pd 3.89 (3.89), Pt 3.92 (3.92). For geometric optimization, ionic forces on each atom were converged to 0.02 eV Å^{-1}. Transition states and activation energies for surface-mediated elementary steps were evaluated using the climbing image nudged elastic band method;[74,75] seven interpolated images and a force convergence criterion of 0.05 eV Å^{-1} were used to calculate activation energies.

The Gaussian 09 simulation package was used to determine solution phase Gibbs free energies.[76] The QB3 variant of complete basis set (CBS) extrapolation method was used; optimizations were performed with the "verytight" convergence criteria.[77,78] The SMD variant of the polarizable continuum model (PCM) with integral equation formalism variant was used to model the presence of water (solvent).[79]

Gibbs free energies of all species were referenced to the gas phase free energies of ccMA and H_2, and the energy of clean slabs:

$$G_{A^\star} = (E_{A^\star} + ZPE_{A^\star} - TS_{A^\star}) - E_{surf} - (E_{MA,g} + ZPE_{MA,g} - TS_{MA,g}) - \frac{m}{2}(E_{H_2,g} + ZPE_{H_2,g} - TS_{H_2,g}) \quad (1)$$

Here, E_i are DFT-calculated total energies, ZPE_i are calculated zero-point energies, and S_i are calculated entropies. Systems denoted with A* contain species A adsorbed on the surface; systems with subscript "g" refer to respective gas-phase quantities (all the required quantities are provided in Tables S1–S6†). E_{surf} is the total energy of the clean slab. The harmonic oscillator approximation was used to calculate ZPE and S. The temperature (T) is 298 K, in accordance with experimental conditions. The constant m corresponds to the stoichiometric coefficient for H_2.

Assuming equilibrium between $H_{2(g)}$ and proton/electron pairs, the computational hydrogen electrode model[80] was used to apply a linear correction to the free energies of faradaic elementary steps:

$$A^\star + (H^+ + e^-) \rightarrow B^\star \quad (2)$$

$$\Delta G(U_{RHE}) = G_{B^\star} - G_{A^\star} + |e|U_{RHE} \quad (3)$$

where U_{RHE} is the electrode potential referenced to the reversible hydrogen electrode (RHE) and e is the electron charge. An additional linear correction term was applied to the DFT-calculated activation free energies ($G_a(U_{0,RHE})$) to account for the applied electrode potential:[48]

$$G_a(U_{RHE}) = G_a(U_{0,RHE}) + \beta^\star(U_{RHE} - U_{0,RHE}) \quad (4)$$

Here, $U_{0,RHE}$ is the onset potential (with the reference to the RHE) for coadsorption of H* (relative to $H_{2(g)}$) in the presence of the reactant molecule for the respective hydrogenation step on a modeled catalyst surface. We assume the value of the symmetry factor (β) to be 0.5, noting potential limitations of this assumption.[81]

Electrode potentials experimentally referenced to the Ag/AgCl electrode were converted to a reference *vs.* the RHE using the following expression: $U_{RHE} = U_{Ag/AgCl} + 0.197 + 0.059 \times pH$. All DFT calculations for H$^+$/e$^-$ transfer steps are accordingly presented at 298 K and $U_{RHE} = -0.14$ V to match the electrode

potential of −0.40 V vs. Ag/AgCl for the bulk electrolysis experiments at pH 1. All elementary reaction energetics are provided in Tables S5–S6.† Due to differences in DFT methods used for calculating solution-phase reaction energetics (hybrid functionals in Gaussian 09) and those at metal surfaces (PBE functionals with plane-wave basis) in Fig. 3 and 4, the thermodynamic cycle must be closed via Hess's law for consistency. We calculated the adsorption energy of ccMA* relative to a gas-phase ccMA reference; these and all subsequent surface-mediated steps were calculated using VASP relative to the common references. We also calculated the energetics of species from ccMA to AA using Gaussian 09 as described above. To maintain consistency of the thermodynamic cycle, we then applied Hess's law to implicitly determine the desorption energies of t2HDA, t3HDA, and AA such that the path to forming each of these species (whether via the surface or solution) has the same net energy change from the ccMA starting point to the given end point. We recognize that this will overestimate the binding strength of ccMA, t2HDA, t3HDA, and AA, as a gas-phase reference for ccMA is more unstable than the "true" reference state, though calculating the appropriate reference energy of ccMA is nontrivial due in part to the low solubility of ccMA in solution. The conclusions of this work are unaffected by the absolute magnitudes of adsorption/desorption energies.

Materials

cis,cis-Muconic acid (ccMA, 97%), adipic acid (AA, 99%), dimethylmalonic acid (DMA, TraceCERT® grade for qNMR), deuterium oxide (D_2O, 99.9 atom% D), potassium sulfate (K_2SO_4, 99%), sulfuric acid-d2 (96–98 wt% in D_2O, 99.5 atom% D) were purchased from Millipore Sigma. trans-3-Hexenedioic acid (t3HDA, 98%) was purchased from Tokyo Chemical Industries. Graphitic carbon felt (0.125 in. thick, 99%) was purchased from Fisher Scientific. Palladium and platinum foils (0.001 in. thick, 99%) were purchased from Fisher Scientific. Pd/C (5 wt%) and Pt/C (5 wt%) powders with average metal particle size ~3 nm were purchased from Millipore Sigma. pH 1 model solutions were prepared by first dissolving a desired amount of ccMA, t3HDA, or AA in deionized (DI) water by ultrasonication; upon dissolution, 18.2 M sulfuric acid (H_2SO_4) was added to obtain an electrolyte concentration of 0.1 M. t2HDA is not commercially available, and therefore, we synthesized it through base-catalyzed isomerization of t3HDA with purity up to 70–80% t2HDA along with t3HDA. Deionized (DI) water (18.2 MΩ cm, Barnstead™ E-Pure™) was used for all experiments in this work.

Electrochemical measurements and reactions

Dissolution of ccMA in H_2SO_4 at pH 1 is notoriously challenging due to its poor solubility,[33] rapid isomerization to ctMA,[82] and progressive acid-catalyzed lactonization to muconolactone.[82,83] We dissolved 50 mg of ccMA in 100 mL of water to remain below the solubility limit of 1 g L^{-1} at pH 1. We found that accelerating the dissolution process with the help of ultrasound mitigated isomerization to ctMA, and maintaining the

temperature at less than 30 °C limited the lactonization process. As such, we managed to consistently prepare stock solutions with <12–18% ctMA and Mlac. Mlac was omitted from the product distribution in Fig. 2, 5, and Fig. S1–S3† as it did not interfere with the hydrogenation reaction and its concentration remained consistent throughout all chronoamperometry experiments. All Mlac was consumed when we performed ccMA ECH at higher catalyst loadings (Fig. S4†).

All electroanalytical measurements and bulk electrolysis were performed using a BioLogic SP-150e potentiostat coupled with a VMP3 10A booster. The uncompensated solution resistance was measured by potentiostatic electrochemical impedance spectroscopy (PEIS) and an 85% iR compensation was applied by the electrochemical workstation to all measurements. A single-compartment 3-electrode setup was used for all electroanalytical measurements (PEIS, LSV, CV). The solution was purged with argon gas before and during measurements. An Ag/AgCl electrode (Pine Research Instrumentations) and a Pt coil served as reference and counter electrodes, respectively. The working electrode consisted of either Pt or Pd foils (2 × 2 cm), or 1 mg of commercial 5 wt% Pt/C or Pd/C ink drop-casted on a glassy carbon electrode.

Bulk electrolysis was performed using a single-compartment ElectroCell MicroFlow Cell® (Amherst, NY) equipped with a Fisherbrand GP1000 peristaltic pump and operated as a loop reactor. A schematic and photographs of the experimental setup are provided in the ESI (Fig. S17†). Pd and Pt foils were attached to a graphite electrode (ElectroCell) using double-sided conductive Cu tape. Pt/C and Pd/C inks were drop casted on a carbon felt (0.125 in) and pressed against the graphite electrode for electrical contact using a PTFE mesh that also served as a turbulence promoter. Platinized titanium was used as a counter electrode, while Ag/AgCl connected to a PTFE separator was used as a reference electrode. The electrode working area was confined to a maximum of 10 cm^2 using EPDM rubber gaskets, which provided additional sealing. The electrode gap was 4 mm and the pump was set to deliver a flow rate of 3 mL s^{-1}, ensuring turbulent conditions.[84] Samples were drawn at regular intervals to record the progress of the reaction. The aliquots were dried in air overnight and then redissolved in an internal standard solution containing DMA dissolved in D_2O. The samples were then analyzed by ^{1}H-NMR using a Bruker 600 MHz spectrometer to identify the product conversion. All calculations were performed on a weight fraction basis.

XRD measurements were performed using a Siemens D500 X-ray diffractometer with a diffracted beam monochromator. To accurately determine possible changes in the H_{UPD} region upon addition of the diacids, we performed the CVs presented in Fig. S11† using 40 wt% Pt/C instead of 5 wt% Pt/C.

Catalyst turnover frequencies were calculated using the rate of the reaction during the first 15 min (TOF = ccMA molecules converted per second per active surface metal site). The catalyst's active sites were calculated from pulsed CO chemisorption using Micromeritics Autochem II 2920. Total active sites

were estimated from the cumulative CO adsorbed and considering the stoichiometric coefficient (1 mol of CO : 2 mol of Pt/Pd).

Author contributions

Deep M. Patel: investigating and validating theoretical calculations on Pd and Pt surfaces; writing – original draft, editing and review. Prathamesh T. Prabhu: investigating and validating electrochemical experiments; writing – editing and review. Geet Gupta: investigating and validating theoretical calculations for the solution phase. Marco Nazareno Dell'Anna: investigating and validating electrochemical experiments; Samantha Kling: investigating and validating electrochemical experiments; Huy Nguyen: investigating and validating electrochemical experiments; Jean-Philippe Tessonnier: conceptualizing, investigating, and supervising the electrochemical experiments; writing – review and editing. Luke T. Roling: conceptualizing, investigating, and supervising the theoretical calculations; writing – review and editing.

Conflicts of interest

All authors of this paper declare that they have no conflicts of interest associated with this work.

Acknowledgements

References

1 D. Vincent Sahayaraj, A. Lusi, A. J. Kohler, H. Bateni, H. Radhakrishnan, A. Saraeian, B. H. Shanks, X. Bai and J.-P. Tessonnier, *Energy Environ. Sci.*, 2023, **16**, 97–112.

2 B. H. Shanks and P. L. Keeling, *Green Chem.*, 2017, **19**, 3177–3185.

3 B. H. Shanks, *Ind. Eng. Chem. Res.*, 2010, **49**, 10212–10217.

4 T. J. Schwartz, B. J. O'Neill, B. H. Shanks and J. A. Dumesic, *ACS Catal.*, 2014, **4**, 2060–2069.

5 B. X. Lee, F. Kjaerulf, S. Turner, L. Cohen, P. D. Donnelly, R. Muggah, R. Davis, A. Realini, B. Kieselbach,

L. S. MacGregor, I. Waller, R. Gordon, M. Moloney-Kitts, G. Lee and J. Gilligan, *J. Public Health Policy*, 2016, **37**, 13–31.

6 J. Iglesias, I. Martínez-Salazar, P. Maireles-Torres, D. Martin Alonso, R. Mariscal and M. López Granados, *Chem. Soc. Rev.*, 2020, **49**, 5704–5771.

7 A. Castellan, J. C. J. Bart and S. Cavallaro, *Catal. Today*, 1991, **9**, 237–254.

8 H. Lü, W. Ren, P. Liu, S. Qi, W. Wang, Y. Feng, F. Sun and Y. Wang, *Appl. Catal., A*, 2012, **441–442**, 136–141.

9 J. Rios, J. Lebeau, T. Yang, S. Li and M. D. Lynch, *Green Chem.*, 2021, **23**, 3172–3190.

10 E. Skoog, J. H. Shin, V. Saez-Jimenez, V. Mapelli and L. Olsson, *Biotechnol. Adv.*, 2018, **36**, 2248–2263.

11 S. M. Zhou, K. Tashiro and T. Li, *Polym. J.*, 2001, **33**, 344–355.

12 W. Deng, Q. Zhang and Y. Wang, *J. Energy Chem.*, 2015, **24**, 595–607.

13 T. Debuissy, E. Pollet and L. Avérous, *J. Polym. Sci., Part A: Polym. Chem.*, 2017, **55**, 1949–1961.

14 X. Zhang, Y. Liu, J. Wang, Y. Zhao and Y. Deng, *J. Microbiol.*, 2020, **58**, 1065–1075.

15 Fortune Business Insights, *Food Service Market Size, Share & COVID-19 Impact Analysis*, Market Research Report, 2022.

16 M. T. Musser, *Ullmann's Encyclopedia of Industrial Chemistry*, Wiley-VCH Verlag GmbH & Co., Hoboken, NJ, USA, 2000.

17 S. R. Nicholson, N. A. Rorrer, T. Uekert, G. Avery, A. C. Carpenter and G. T. Beckham, *ACS Sustainable Chem. Eng.*, 2023, **11**, 2198–2208.

18 S. Gundekari, B. Biswas, T. Bhaskar and K. Srinivasan, *Biomass Bioenergy*, 2022, **161**, 106448.

19 M. Lang and H. Li, *ChemSusChem*, 2022, **15**, e202101531.

20 B. H. Shanks and L. J. Broadbelt, *ChemSusChem*, 2019, **12**, 2970–2975.

21 A. E. Settle, L. Berstis, N. A. Rorrer, Y. Roman-Leshkóv, G. T. Beckham, R. M. Richards and D. R. Vardon, *Green Chem.*, 2017, **19**, 3468–3492.

22 B. Hočevar, A. Prašnikar, M. Huš, M. Grilc and B. Likozar, *Angew. Chem., Int. Ed.*, 2021, **60**, 1244–1253.

23 A. Corona, M. J. Biddy, D. R. Vardon, M. Birkved, M. Z. Hauschild and G. T. Beckham, *Green Chem.*, 2018, **20**, 3857–3866.

24 D. R. Vardon, M. A. Franden, C. W. Johnson, E. M. Karp, M. T. Guarnieri, J. G. Linger, M. J. Salm, T. J. Strathmann and G. T. Beckham, *Energy Environ. Sci.*, 2015, **8**, 617–628.

25 G. Wang, S. Øzmerih, R. Guerreiro, A. C. Meireles, A. Carolas, N. Milne, M. K. Jensen, B. S. Ferreira and I. Borodina, *ACS Synth. Biol.*, 2020, **9**, 634–646.

26 T. Liu, B. Peng, S. Huang and A. Geng, *Bioresour. Technol. Rep.*, 2020, **9**, 100395.

27 R. Sillers, R. Hermann, M. Spencer, R. Udani and R. R. Yocum, US 2021/0277429 A1, 2021.

28 X. She, H. M. Brown, X. Zhang, B. K. Ahring and Y. Wang, *ChemSusChem*, 2011, **4**, 1071–1073.

29 S. Capelli, A. Rosengart, A. Villa, A. Citterio, A. Di Michele, C. L. Bianchi, L. Prati and C. Pirola, *Appl. Catal., B*, 2017, **218**, 220–229.

30 S. Capelli, D. Motta, C. Evangelisti, N. Dimitratos, L. Prati, C. Pirola and A. Villa, *ChemCatChem*, 2019, **11**, 3075–3084.

31 A. E. Settle, N. S. Cleveland, C. A. Farberow, D. R. Conklin, X. Huo, A. A. Dameron, R. W. Tracy, R. Sarkar, E. J. Kautz, A. Devaraj, K. K. Ramasamy, M. J. Watson, A. M. York, R. M. Richards, K. A. Unocic, G. T. Beckham, M. B. Griffin, K. E. Hurst, E. C. D. Tan, S. T. Christensen and D. R. Vardon, *Joule*, 2019, **3**, 2219–2240.

32 M. Suastegui, J. E. Matthiesen, J. M. Carraher, N. Hernandez, N. Rodriguez Quiroz, A. Okerlund, E. W. Cochran, Z. Shao and J.-P. Tessonnier, *Angew. Chem., Int. Ed.*, 2016, **55**, 2368–2373.

33 M. N. Dell'Anna, M. Laureano, H. Bateni, J. E. Matthiesen, L. Zaza, M. P. Zembrzuski, T. J. Paskach and J.-P. Tessonnier, *Green Chem.*, 2021, **23**, 6456–6468.

34 J. E. Matthiesen, J. M. Carraher, M. Vasiliu, D. A. Dixon and J.-P. Tessonnier, *ACS Sustainable Chem. Eng.*, 2016, **4**, 3575–3585.

35 M. N. Dell'Anna, G. Gupta, P. T. Prabhu, T.-H. Chu, L. T. Roling and J.-P. Tessonnier, *Green Chem.*, 2023, **25**, 10387–10397.

36 S. Abdolmohammadi, D. Gansebom, S. Goyal, T. H. Lee, B. Kuehl, M. J. Forrester, F. Y. Lin, N. Hernández, B. H. Shanks, J.-P. Tessonnier and E. W. Cochran, *Macromolecules*, 2021, **54**, 7910–7924.

37 J. T. Bender, A. S. Petersen, F. C. Østergaard, M. A. Wood, S. M. J. Heffernan, D. J. Milliron, J. Rossmeisl and J. Resasco, *ACS Energy Lett.*, 2023, **8**, 657–665.

38 K. S. Exner, *Curr. Opin. Electrochem.*, 2021, **26**, 100673.

39 D. Wei, X. Shi, P. Sponholz, H. Junge and M. Beller, *ACS Cent. Sci.*, 2022, **8**, 1457–1463.

40 M. A. Khan, T. A. Al-Attas, N. G. Yasri, H. Zhao, S. Larter, J. Hu and M. G. Kibria, *Sustainable Energy Fuels*, 2020, **4**, 5568–5577.

41 H. Luo, J. Barrio, N. Sunny, A. Li, L. Steier, N. Shah, I. E. L. Stephens and M.-M. Titirici, *Adv. Energy Mater.*, 2021, **11**, 2101180.

42 Q. Yu and J. M. Bowman, *J. Chem. Theory Comput.*, 2016, **12**, 5284–5292.

43 J. K. Nørskov, T. Bligaard, B. Hvolbæk, F. Abild-Pedersen, I. Chorkendorff and C. H. Christensen, *Chem. Soc. Rev.*, 2008, **37**, 2163–2171.

44 N. Singh, U. Sanyal, G. Ruehl, K. A. Stoerzinger, O. Y. Gutiérrez, D. M. Camaioni, J. L. Fulton, J. A. Lercher and C. T. Campbell, *J. Catal.*, 2020, **382**, 372–384.

45 J. Park and L. T. Roling, *AIChE J.*, 2020, **66**, e17036.

46 B. Tran, Y. Cai, M. J. Janik and S. T. Milner, *J. Phys. Chem. A*, 2022, **126**, 7382–7398.

47 J. Ekspong, E. Gracia-Espino and T. Wågberg, *J. Phys. Chem. C*, 2020, **124**, 20911–20921.

48 S. A. Akhade, N. J. Bernstein, M. R. Esopi, M. J. Regula and M. J. Janik, *Catal. Today*, 2017, **288**, 63–73.

49 J. Li, J. H. Stenlid, T. Ludwig, P. S. Lamoureux and F. Abild-Pedersen, *J. Am. Chem. Soc.*, 2021, **143**, 19341–19355.

50 H. J. Peng, M. T. Tang, J. Halldin Stenlid, X. Liu and F. Abild-Pedersen, *Nat. Commun.*, 2022, **13**, 1–11.

51 J.-P. Tessonnier, B. H. Shanks, E. W. Cochran, J. E. Hadel, M. N. Dell'Anna, P. Carter and D. Gansebom, WO-2022061275-A1, 2022.

52 N. Singh, U. Sanyal, J. L. Fulton, O. Y. Gutiérrez, J. A. Lercher and C. T. Campbell, *ACS Catal.*, 2019, **9**, 6869–6881.

53 I. K. M. Yu, F. Deng, X. Chen, G. Cheng, Y. Liu, W. Zhang and J. A. Lercher, *Nat. Commun.*, 2022, **13**, 7154.

54 S. F. Yuk, M.-S. Lee, S. A. Akhade, M.-T. Nguyen, V.-A. Glezakou and R. Rousseau, *Catal. Today*, 2022, **388–389**, 208–215.

55 K. Hayashi, S. Kameoka and A.-P. Tsai, *Mater. Trans.*, 2021, **62**, 1089–1096.

56 M. Yuan, K. Lee, D. G. Van Campen, S. Liguori, M. F. Toney and J. Wilcox, *Ind. Eng. Chem. Res.*, 2019, **58**, 926–934.

57 A. L. Cabrera, E. Morales-Leal, J. Hasen and I. K. Schuller, *Catal. Lett.*, 1994, **30**, 11–23.

58 L. C. Yule, E. Daviddi, G. West, C. L. Bentley and P. R. Unwin, *J. Electroanal. Chem.*, 2020, **872**, 114047.

59 N. M. Marković, B. N. Grgur and P. N. Ross, *J. Phys. Chem. B*, 1997, **101**, 5405–5413.

60 F. Sanchez, D. Motta, A. Roldan, C. Hammond, A. Villa and N. Dimitratos, *Top Catal.*, 2018, **61**, 254–266.

61 C. J. Bondue, F. Calle-Vallejo, M. C. Figueiredo and M. T. M. Koper, *Nat. Catal.*, 2019, **2**, 243–250.

62 M. Smiljanić, M. Bele, L. Moriau, F. Ruiz-Zepeda, M. Šala and N. Hodnik, *J. Phys. Chem. C*, 2021, **125**, 27534–27542.

63 M. Jin, H. Zhang, Z. Xie and Y. Xia, *Energy Environ. Sci.*, 2012, **5**, 6352–6357.

64 G. Kresse and J. Furthmüller, *Comput. Mater. Sci.*, 1996, **6**, 15–50.

65 G. Kresse and J. Furthmüller, *Phys. Rev. B: Condens. Matter Mater. Phys.*, 1996, **54**, 11169–11186.

66 P. E. Blöchl, *Phys. Rev. B: Condens. Matter Mater. Phys.*, 1994, **50**, 17953–17979.

67 G. Kresse and D. Joubert, *Phys. Rev. B: Condens. Matter Mater. Phys.*, 1999, **59**, 1758–1775.

68 J. P. Perdew, J. A. Chevary, S. H. Vosko, K. A. Jackson, M. R. Pederson, D. J. Singh and C. Fiolhais, *Phys. Rev. B: Condens. Matter Mater. Phys.*, 1992, **46**, 6671–6687.

69 S. Grimme, J. Antony, S. Ehrlich and H. Krieg, *J. Chem. Phys.*, 2010, **132**, 154104.

70 S. Grimme, S. Ehrlich and L. Goerigk, *J. Comput. Chem.*, 2011, **32**, 1456–1465.

71 L. Bengtsson, *Phys. Rev. B: Condens. Matter Mater. Phys.*, 1999, **59**, 12301–12304.

72 H. J. Monkhorst and J. D. Pack, *Phys. Rev. B: Solid State*, 1976, **13**, 5188–5192.

73 *CRC Handbook of Chemistry and Physics*, ed. W. M. Haynes, CRC Press, Boca Raton, Florida, 97th edn, 2016.

74 G. Henkelman, B. P. Uberuaga and H. Jónsson, *J. Chem. Phys.*, 2000, **113**, 9901–9904.

75 G. Henkelman and H. Jónsson, *J. Chem. Phys.*, 2000, **113**, 9978–9985.

76 M. J. Frisch, G. W. Trucks, H. B. Schlegel, G. E. Scuseria, M. A. Robb, J. R. Cheeseman, G. Scalmani, V. Barone, B. Mennucci, G. A. Petersson, H. Nakatsuji, M. Caricato, X. Li, H. P. Hratchian, A. F. Izmaylov, J. Bloino, G. Zheng, J. L. Sonnenberg, M. Hada, M. Ehara, K. Toyota, R. Fukuda, J. Hasegawa, M. Ishida, T. Nakajima, Y. Honda, O. Kitao, H. Nakai, T. Vreven, J. A. Montgomery Jr., J. E. Peralta, F. Ogliaro, M. Bearpark, J. J. Heyd, E. Brothers, K. N. Kudin, V. N. Staroverov, T. Keith, R. Kobayashi, J. Normand, K. Raghavachari, A. Rendell, J. C. Burant, S. S. Iyengar, J. Tomasi, M. Cossi, N. Rega, J. M. Millam, M. Klene, J. E. Knox, J. B. Cross, V. Bakken, C. Adamo, J. Jaramillo, R. Gomperts, R. E. Stratmann, O. Yazyev, A. J. Austin, R. Cammi, C. Pomelli, J. W. Ochterski, R. L. Martin, K. Morokuma, V. G. Zakrzewski, G. A. Voth, P. Salvador, J. J. Dannenberg, S. Dapprich, A. D. Daniels, O. Farkas, J. B. Foresman, J. V. Ortiz, J. Cioslowski and D. J. Fox, *Gaussian 09, Revision E.01*, Wallingford CT, 2013.

77 A. D. McLean and G. S. Chandler, *J. Chem. Phys.*, 1980, **72**, 5639–5648.

78 K. Raghavachari and G. W. Trucks, *J. Chem. Phys.*, 1989, **91**, 1062–1065.

79 A. V. Marenich, C. J. Cramer and D. G. Truhlar, *J. Phys. Chem. B*, 2009, **113**, 6378–6396.

80 J. K. Nørskov, J. Rossmeisl, A. A. Logadottir, L. Lindqvist, J. R. Kitchin, T. Bligaard and H. Jónsson, *J. Phys. Chem. B*, 2004, **108**, 17886–17892.

81 A. Rendón-Calle, Q. H. Low, S. H. L. Hong, S. Builes, B. S. Yeo and F. Calle-Vallejo, *Appl. Catal., B*, 2021, **285**, 119776.

82 J. M. Carraher, T. Pfennig, R. G. Rao, B. H. Shanks and J.-P. Tessonnier, *Green Chem.*, 2017, **19**, 3042–3050.

83 J. M. Carraher, P. Carter, R. G. Rao, M. J. Forrester, T. Pfennig, B. H. Shanks, E. W. Cochran and J.-P. Tessonnier, *Green Chem.*, 2020, **22**, 6444–6454.

84 S. J. C. Weusten, J. van der Schaaf and M. T. de Groot, *J. Electroanal. Chem.*, 2022, **918**, 116481.